

# Simulation-based failure analysis of faulty and regulatory railhead repair welding procedures

Downloaded from: https://research.chalmers.se, 2025-10-30 19:53 UTC

Citation for the original published paper (version of record):

Andersson, B., Josefson, L. (2025). Simulation-based failure analysis of faulty and regulatory railhead repair welding procedures. Engineering Failure Analysis, 182. http://dx.doi.org/10.1016/j.engfailanal.2025.110185

N.B. When citing this work, cite the original published paper.

research.chalmers.se offers the possibility of retrieving research publications produced at Chalmers University of Technology. It covers all kind of research output: articles, dissertations, conference papers, reports etc. since 2004. research.chalmers.se is administrated and maintained by Chalmers Library

FISEVIER

Contents lists available at ScienceDirect

### **Engineering Failure Analysis**

journal homepage: www.elsevier.com/locate/engfailanal



## Simulation-based failure analysis of faulty and regulatory railhead repair welding procedures

Björn Andersson<sup>®</sup>\*, B. Lennart Josefson<sup>®</sup>

Department of Industrial and Materials Science, Chalmers University of Technology, Gothenburg, Sweden



#### ARTICLE INFO

Keywords:
Welding simulation
Rail defect repair
Numerical simulations
Phase transformation
Residual stress
Over-rolling simulation

#### ABSTRACT

Advancements in railway technology have significantly reduced wheel and axle failures, yet rail failures, particularly in welded regions, remain a major concern. Up to 60% of recorded rail failures occur in these areas, with accident reports frequently attributing incidents to improperly executed repair welds. Using thermo-metallurgical-mechanical finite element simulations, this study investigates the mechanical performance of regulatory and faulty in-situ railhead repair welds, where only part of the railhead is removed. The multi-pass welding simulations employ a multi-phase homogenization-based material model, incorporating non-linear isotropic and kinematic hardening, phase transformation kinetics, and virgin material state recovery. Mechanical performance of the railhead repairs is evaluated through wheel-rail contact over-rolling simulations and fatigue analysis using novel multi-phase Dang Van criterion.

The comparison, based on quantitative data, reveals an increased risk of fatigue crack initiation when deviations from the regulatory procedure occur. The regulatory repair produces a ferritic-pearlitic microstructure and a more favorable residual stress state, characterized by compressive stresses in the weld region and tensile stresses deeper below the rail surface where the microstructure is more favorable. In contrast, the faulty repair exhibits rapid cooling rates, leading to brittle martensitic phases and high tensile residual stresses near the rail surface, significantly increasing fatigue crack initiation risk. Operational over-rolling simulation further demonstrate that tensile stresses in the faulty repair persist near the surface, failing to redistribute as effectively as in the regulatory repair. These findings underscore the importance of strict adherence to repair welding standards to prevent premature rail failures and costly maintenance interventions.

#### 1. Introduction

Rail transport is essential for sustainable mobility, offering low CO<sub>2</sub> emissions and high efficiency [1–3]. However, the ongoing shift towards increased rail transport necessitates higher axle loads, speeds, and traffic density, which intensifies mechanical loads on the rail and accelerates fatigue damage and surface wear [4–6]. This growing demand underscores the need for effective rail maintenance, where railhead repair welding serves as a cost-effective alternative to rail replacement when repairing rail surface damage, while minimizing operational disruptions [7–9]. To ensure long-term durability, regulatory repair welding procedures prescribe strict guidelines for material removal, preheating, and weld procedure [10,11]. However, reports from incidents of fractured rails often indicate deviations from these procedures, raising concerns about the structural integrity of faulty repair welds. To address this issue, this study uses numerical tools to compare the performance of a faulty and a regulatory railhead repair welding.

E-mail address: abjorn@chalmers.se (B. Andersson).

https://doi.org/10.1016/j.eng fail anal. 2025.110185

Received 22 April 2025; Received in revised form 1 October 2025; Accepted 3 October 2025

<sup>\*</sup> Corresponding author.

Field observations and maintenance statistics highlight the critical role of welds in rail performance, as a disproportionate share of defects occur in or near welded regions [12]. Swedish railway data report that 20%–60% of all rail defects are located close to welds, with 60% of defects requiring urgent repair within a week and 20% considered non-critical [13]. In 2022 alone, 435 welding-related defects were recorded. This overrepresentation of failures in welded regions is linked the harsh wheel–rail contact conditions, which involve high contact pressures [14–16] and millions of load cycles [17–19], possibly amplified by both surface irregularities [20,21] and residual stresses [22,23] from welding. Nevertheless, repair welds are integral to regular maintenance [24,25]. While shallow defects such as surface wear or cracks can be addressed through cladding, see e.g. [26,27], or using grinding or milling, see e.g. [28,29], deeper cracks must be addressed by removing damaged material. Either by replacing entire rail segments using flash-butt or aluminothermic (thermite) welding, see e.g. [30,31], or by in-situ railhead repair via arc-welding, see e.g. [32].

Although flash-butt and thermite welds are more labor-intensive, these procedures are inherently more robust as these involves uniform and significantly stronger heating. Whereas railhead repair welds are performed in situ and involves highly localized heating, remelting, and rapid cooling. This introduces complex thermo-mechanical conditions which include risks of martensitic transformation and tensile residual stresses [33], as well as weld-induced imperfections such as porosity, inclusions, and geometric irregularities [34]. To mitigate these risks, adherence to aforementioned guidelines is essential. However, several fracture investigations [35–37] confirm that non-regulatory railhead repair procedures are used in practice. This raises the critical question of how such deviations impact rail surface's mechanical performance.

While the mechanical performance of flash-butt welding and thermite welding has been extensively studied, see e.g. [38–40] and [41–43] respectively, railhead repair welding has not been investigated to the same extent. In fact, previous repair welding research has only followed different standardized welding procedures and focused on aspects such as material phases and residual stresses of the heat-affected zone [44–47]. Comparative studies evaluating the performance of regulatory and faulty railhead repair welding procedures are lacking. The present study aims to address this knowledge gap by systematically comparing the Swedish regulatory repair welding procedure [10,11] to a generic representation of a faulty repair. Given that faulty repairs occur and the absence of research on their mechanical consequences, it is imperative to assess their impact on residual stress distributions, microstructure evolution, and fatigue performance under operational loading conditions.

To asses this, a finite element (FE) modeling approach is employed to simulate the multi-pass railhead repair welding process and evaluate the mechanical response of the two repair welding procedures. This simulation framework, developed and validated in previous works [48–51], further adds to existing research [44–46] using more advanced material modeling [48,50], more detailed welding simulations [49] and more comprehensive fatigue evaluation of multi-phase material states. In summary, the framework includes multi-phase homogenization-based material modeling with non-linear kinematic and isotropic hardening, combined 3D and 2D extended generalised plane strain (GPS) modeling for welding and over-rolling simulations in which mechanical performance is evaluated using a novel homogenization based Dang Van stress fatigue evaluation.

Furthermore, to ensure the applicability of the simulation framework to the faulty repair welding procedure, the study also includes an appended validation of the methodology through a 2D GPS vs. 3D simulation comparison of the mechanical analysis. While not the primary research objective, this appended comparison contributes significantly to the methodological framework, underscoring the reliability of the simulation approach employed in this study.

This study offers insights into improving railway maintenance strategies by using state-of-the-art simulations to demonstrate the increased risk of fatigue crack initiation associated with faulty in-situ repair welding, an issue is often observed in practice but hitherto not studied. The findings emphasize the importance of strict adherence to regulatory procedures, improved quality control measures, and sufficient scheduling for proper repair execution. Ensuring that repair welders follow best practices is essential to mitigating long-term rail degradation and reducing the frequency of weld-related failures. The insights gained from this study can inform infrastructure managers, railway operators, and maintenance personnel, helping to enhance inspection protocols, repair guidelines, and track maintenance policies.

#### 2. Railhead repair welding process

An important objective of railway infrastructure maintenance is to ensure the structural robustness and longevity of railway tracks. Localized rail surface damage, such as cracks, squats, wheel-burns, or other defects that compromise rail integrity, can be repaired efficiently using in-situ railhead repair welding [7–9] instead of replacing entire rail sections. The Swedish regulations for stick welding railhead repairs [10,52,53] (and the European equivalent [11]) outline a standardized procedure to remove damaged material and restore the structural integrity and mechanical performance of the rail. However, failure reports on damaged repair welded rail frequently indicate that deviations from these prescribed procedures lead to sub-optimal repairs [35–37], increasing the risk of crack initiation and propagation, and in severe cases, rail fractures. This section describes both the regulatory welding procedure and a generic description of a faulty repair, based on commonly observed regulatory deviations. In the present study, both procedures are employed to address a specific case of localized surface damage to the running band of the railhead, such as a squat, wheel-burn, head checks or surface crack, of a rail of steel grad R260 and rail profile 60E1 [54].

#### 2.1. Regulatory railhead repair welding procedure

The Swedish regulatory in-situ railhead repair welding process [10,52,53] consists of several well-defined steps to ensure a structurally sound and durable repair. First, the damaged section of the railhead is identified and removed using milling or cutting techniques to ensure complete removal of the defective material. Importantly, the cut-out is performed with a trapezoidal shape

Table 1
Chemical composition of R260 rail steel [54] and weld filler material ESAB OK30 Weartrode [57].

	С	Mn	Si	P	Mo	S	Cr	Al	V	Fe
R260	060-0.82	0.65-1.25	0.16-0.60	≤0.03	≤ 0.08	≤0.03	≤0.15	≤0.004	≤0.03	bal.
Weartrode	0.1	0.7	0.7	_	-	_	3.2	-	_	bal.

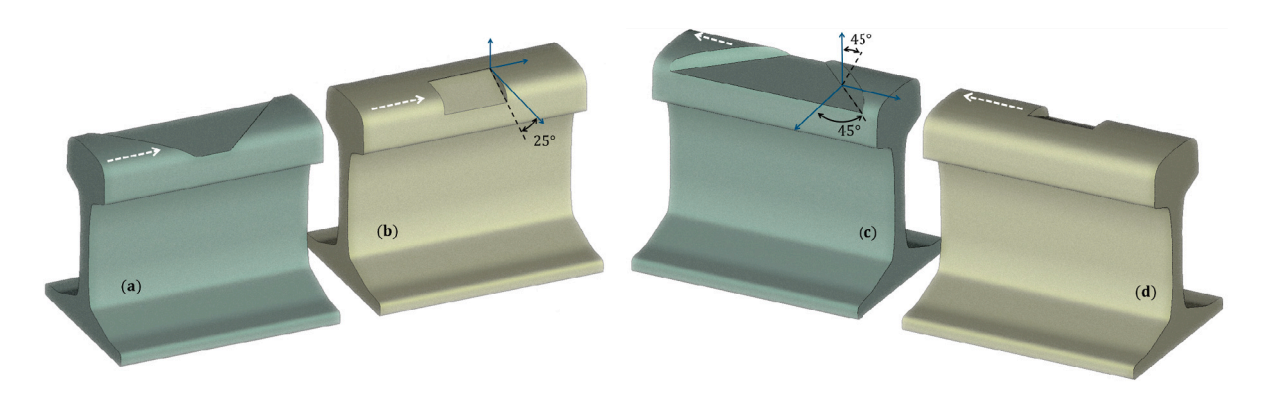


Fig. 1. (a) & (c) Illustration of railhead repair cutout following the regulatory procedure, highlighting the cutout angles. (b) & (d) Generic illustration of a typical faulty repair railhead cut out. Arrows indicate suggested position of the train wheel flange.

at a 45° angle relative to both the vertical and axial directions, as illustrated in Figs. 1a and 1c. The chamfered edges of the trapezoidal cut-out facilitate a smoother transition between the repaired section and the base material under operational loading, which minimizes the stress concentrations and reduces the risk of crack formation. Moreover, the orientation of the cut-out relative to the railway track is a critical aspect of the regulatory repair process, as can be concluded from the findings in [47]. By orienting the short edge of the trapezoidal cut-out to face inward in track, the train wheel passes over this shorter edge, highlighted by dashed arrows in Fig. 1. This edge experiences slower cooling than the start and end sections of the longer edge and therefore experiences less risk of unfavorable, brittle microstructures.

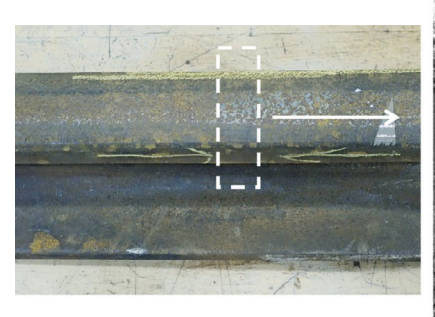
Following material removal, the welding area is prepared by detaching adjacent sleepers and raising the rail to provide unobstructed access. To minimize the effects of steep temperature gradients during welding, the rail is preheated to 350 °C using a propane torch. The preheated region includes the cut-out and extends 100 mm on either side and, to ensure a uniform thermal distribution, also includes the railhead, web, and rail foot. Next, the welding procedure starts with longitudinal weld passes along the edges of the cut-out to create structural support ridges. This is followed by high-power zig-zag passes that fill the gap between the ridges. If the rail temperature falls below the operational threshold of 300 °C, additional propane torch reheating is applied before proceeding with further weld passes. This sequence ensures strong heat input, ideal material deposition, and optimal mechanical performance of the repaired rail section. After completing the welding, the rail is left to cool naturally in ambient conditions, shielded from wind and draft. High-strength rail steels or colder climates, which are not the focus of this study, require insulating blankets to reduce thermal gradients. After cooling, excess material is removed through grinding, to restore the original railhead geometry. The final step involves non-destructive testing (NDT), including visual and ultrasonic inspection, to detect potential surface or subsurface defects, ensuring the structural integrity of the repair [55].

The welding performed using ESAB OK Wartrode 30 as the filler material [56,57]. The selection of this specific filler material is due to its ability to produce a surface hardness that is compatible with R260 rail steel. A comparison of the chemical composition of the two materials is provided in Table 1. In addition, typical value for the room temperature yield stress of R260 is 560 MPa and the same mechanical properties are assumed for the filler material.

#### 2.2. Faulty repair procedure

A review of field failure reports reveals that deviations from the regulatory repair welding procedure are frequently observed in repair-welded rails [35,36], compromising the integrity and durability of the repair. Two illustrative cases are presented in Figs. 2 and 3. In both cases, the material removal has been found to be shallow, and the crack propagation benchmarks indicates that the fatigue cracks have originated in the weld-base material fusion zone, i.e. subsurface cracks, where there is large differences in the microstructure. While a multitude of deviation patterns may be observed, the most prevalent suboptimal repairs are attributed to three fundamental deficiencies: inadequate material removal, improper welding execution, and insufficient preheating, as described in the following sections.

Firstly, in contrast to the trapezoidal cut-out used in the regulatory repair, only the damaged material at the gauge corner of the railhead is removed, as illustrated in Figs. 1b and 1d. This cut-out is significantly smaller and shallower, increasing the risk that pre-existing cracks or subsurface damage remain within the rail. Any residual defects left in place can rapidly propagate under operational loading, reducing the structural reliability of the repair. Furthermore, as a less weld filler material is deposited to fill



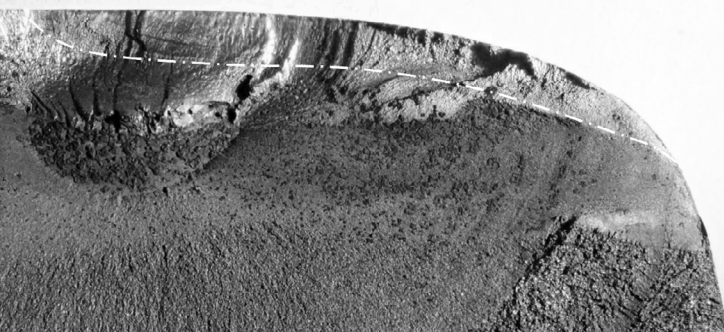


**Fig. 2.** Repair welded railhead which as fractured due to vertical crack. Cross-sectional view of the fracture surface show that the crack originated from the fusion zone, highlighted by the dot-dashed line. *Source:* From: [35].

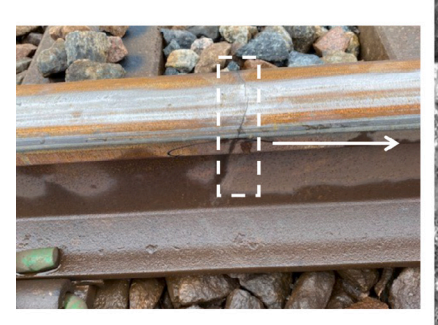




**Fig. 3.** Repair welded railhead which as fractured due to vertical crack. Cross-sectional view of the fracture surface show that the crack originated from the incomplete removal of preexisting crack. The fusion zone is highlighted by the dot-dashed line. *Source:* From: [36].

this smaller gap, there is a significant reduction in heat input to the railhead. This results in higher cooling rates and an increased risk of unfavorable brittle microstructures.

Secondly, deviations from the prescribed welding sequence are commonly observed. Instead of performing longitudinal support weld passes followed by high-power zig-zag welds in between, a simplified and less robust pattern is often used. This typically only consists of zig-zag passes, applied either longitudinally or transversely and can lead to inconsistent material deposition, less heat input, and faster cooling rates. Importantly, as stated above, less heat input causes rapid cooling and increases the likelihood of martensite formation. Additionally, if residual cracks remain due to inadequate material removal, the combination of tensile residual stress and brittle martensitic transformation can further accelerate crack growth.

Thirdly, insufficient preheating or poor operational temperature monitoring are a critical factors that adversely affects quality repair. Without sufficient preheating or reheating, more rapid cooling during welding may result in excessive temperature gradients, again, promoting brittle microstructures and locally increased residual stress levels.

#### 3. Method

This section describes the method employed to assess the impact of sub-optimally performed railhead repairs compared to repairs following the regulatory procedure. Key differences in residual stress distributions, microstructural transformations, and fatigue crack initiation under operational conditions are analyzed using a simulation methodology developed in a previous work [49]. Additionally, to ensure the accuracy of the simulation methodology, its 2D GPS mechanical simulation (see Section 4.2) is further validated by comparing it to 3D mechanical simulations for the faulty repair process.

#### 3.1. Procedure for comparing regulatory and faulty repairs

The regulatory and faulty repair procedures presented in Fig. 1 are compared, focusing on the material state following the repair welding and the mechanical performance of the repaired rail section under operational over-rolling loads. Firstly, the welding simulations primarily assess differences in the residual stress field and microstructure resulting from differences in heat input and

material deposition for the regulatory and faulty repair procedures. Particular attention is given to phase transformations that may introduce brittle regions, as well as the presence of tensile residual stresses, both of which can significantly increase the risk of fatigue failure. Secondly, the redistribution of residual stresses as train wheels traverse the repaired rail section is analyzed to provide insights into the mechanical performance of both the regulatory and faulty repairs. In addition to stress field comparisons, the risk of fatigue crack initiation is evaluated using the Dang Van multiaxial fatigue criterion, allowing for a quantitative assessment of differences in fatigue performance between the two repair methods. However, growth of macroscopic cracks from these defects and estimations of remaining life are outside the scope of the study.

This systematic comparison of faulty and regulatory repair welding procedures aims to identify regions most susceptible to failure and emphasize the critical importance of adhering to established railhead repair welding regulations. Mainly by highlighting the potential risks associated with deviations from these guidelines, underscoring the detrimental impact that sub-optimal repair practices may have on rail integrity and service life.

#### 3.2. 2D vs 3D validation for faulty repairs

The 2D simulation methodology for the mechanical analysis developed in [47,49] has been demonstrated to be accurate in simulations of railhead repair welding procedures where the railhead repair geometry is symmetric. However, the railhead geometry of the faulty repair is asymmetric and the methodology therefore requires further validation to ensure the accuracy. To this end, a direct comparison between the 2D simulation methodology and a 3D simulation of a faulty repair is presented in Appendix. Unlike the regulatory railhead repair welding procedure, the geometry of the faulty repair involves minimal material removal, restricted to the gauge corner, and includes fewer weld passes. Consequently, the FE model of faulty repair is smaller, thereby facilitating the execution of comprehensive 3D mechanical simulations. These simulations would otherwise incur excessive costs for the multi-pass welding process employed in regulatory repairs.

The appended validation procedure compares the residual stress fields between the 2D and 3D models within the repaired region. Additionally, transient stress-time histories, evaluated at specific locations, are compared to ensure that the 2D model accurately captures stress evolution throughout the welding process. The objective of this validation is to demonstrate that the 2D mechanical simulation methodology replicates key trends observed in the 3D analysis while offering significantly reduced computational costs, thereby establishing it as a viable tool for comparative assessments of repair welding procedures, and also to carry out studies for finding improved of rail repair welding procedures and process parameters.

#### 4. Finite element model and simulation setup

This section describes the FE model and simulation setups, including the simulation methodology for repair welding, over-rolling simulations, and material modeling, as well as the 3D and 2D simulations used in the study.

#### 4.1. Simulation methodology

#### 4.1.1. Material model

Repair welding exposes the rail material to multiple localized heating cycles, as each weld pass induces heating, (re)melting, solidification, and phase transformations and requires thermo-mechanical-metallurgical material modeling. A detailed description of the implementation of the metallurgical modeling, i.e. the phase transformation kinetics, is provided in a previous work [50] and the references therein. In short, the modeling includes heating-induced austenitization, cooling-driven martensite and bainite formation, and subsequent tempering or re-melting of the material. The kinetics of these transformations are modeled using established analytically based methods, including the Johnson-Mehl-Avrami-Kolmogorov (JMAK) equation for diffusive phase transformations and the Koistinen-Marburger equation for displacive martensitic transformations. The transformation kinetics modeling is validated against dilatation experiments in [50], representing spot-heating of a train wheel at braking, and against hardness and microstructure measurements of a railhead weld repair experiment in [47], representing the repairing of a frog of a rail crossing switch using process parameters according to regulations [10,52,53].

The constitutive model, is described in full detail in a previous work [48] and validated against residual stresses measurements in a laser spot-flash-heating experiment using R260 rail. This model captures the material's multi-phase behavior during welding by employing a self-consistent multi-phase homogenization of the individual phases' mechanical material response, see e.g. [58,59]. This homogenization allows for simultaneous elastic and plastic deformations in material phases of significantly different ductility. Each material phase is modeled by individual constitutive material models, run in parallel. The constitutive models assumes additive decomposition of the total strain, see e.g. [60], and uses a Chaboche plasticity model, see e.g. [61], with non-linear kinematic and isotropic hardening, [62]. Transformation-induced plasticity (TRIP) effects, see e.g. [63,64], are also included, as well as virgin material state recovery upon melting, see e.g. [65,66].

All material parameters are assumed to be temperature-dependent, with values adopted from [50] and linearly extrapolated to the temperature range considered in this study. This comprehensive modeling framework, implemented as user-defined subroutines in the commercial software Abaqus [67], ensures a realistic representation of the cyclic heating and cooling effects inherent in multi-pass repair welding processes.

#### 4.1.2. Welding simulation

The repair welding simulation methodology used is described in detail in a previous work [49], in which the residual stress profile is validated against residual stress measurements from a full-scale Korean repair welding procedure [46]. Moreover, the welding process simulation is validated using hardness measurements and microstructure evaluations in aforementioned railhead weld repair experiment [47]. Additionally, in [51] the welding simulations are validated against experimentally determined residual stresses, where a laser fusion heat source heated a rail material sample in multi-pass welding. The methodology uses a one-way coupled 3D transient thermal analysis and a 2D quasi-static mechanical analysis. In short, the 3D thermal analysis uses a moving double ellipsoid heat source [68] calibrated in a previous work [47] based on experimental data to ensure accurate representation of heat input, phase transformations, and material deposition. During the simulation, weld filler material is added incrementally using the silent element activation approach, see e.g. [69], implemented together with the moving heat source in user-defined subroutines.

Furthermore, the subsequent 2D mechanical analysis is performed using a Generalized Plane Strain (GPS) model, which has been extended to incorporate the out-of-plane axial and bending stiffnesses of the rail. This FE-element implementation assumes constant curvature in the out-of-plane direction and that the cross-section lies between two rigid bounding planes. These planes are capable of rotating around the in-plane horizontal and vertical axes about a predefined pivot point and of translating axially along the out-of-plane axis, i.e. longitudinal direction of the rail. Assigning stiffness constraints to these axial and bending degrees of freedom, allow for efficient yet accurate predictions of residual stress distributions in the rail. However, it is important to note that these constraints are derived from the symmetry of the rail cross-section and the axial nature of the rail. Consequently, the in-plane symmetry of the regulatory repair makes its geometry more suitable for this simulation methodology than the in-plane asymmetry of the faulty repair, see Fig. 1, hence the need for the additional 2D model validation presented in this study, see Appendix.

#### 4.1.3. Over-rolling simulation

In order to replicate a 3D Hertzian contact pressure distribution of a wheel traversing the rail surface in 2D, the 2D GPS model is modified using a piecewise linear scaling profile for element thicknesses, as described in [47,70]. This scaling ensures that the maximum von Mises stress distribution, measured along a path from the rail foot to the contact position, closely resembles that of a 3D model. The setup uses parts of the multi-step over-rolling simulation methodology presented in [71]. Furthermore, due to the 2D assumption, only normal contact pressure and transverse traction forces are applied. This method effectively reproduces the outcomes of a full-scale 3D over-rolling simulation with high accuracy while significantly reducing computational costs and is qualitatively validated in terms of identifying regions critical for fatigue crack initiation [47].

The applied load sequence is derived from 483 measured wheel passages recorded on a curved rail section (steel grade 260 and railprofile 60E1 [54]) along the Western Main Line in Sweden, between Nyckelsjön and Sparreholm [72]. The dataset consists of 90% passenger trains, with axle loads ranging from 11.7 to 21.0 tonnes, and 10% freight trains, with an axle load of 22.5 tonnes. To simulate long-term operational conditions, the sequence is repeated multiple times to generate thousands of over-rolling events. However, it should be noted that the load sequence represents non-welded rail, and its repetitions do not incorporate regenerating or updating of the load sequence. This means that any potential effects from welds in the rail, such as increased surface wear, see e.g. [20], causing variations in contact position or dynamic load magnification effects, see e.g. [73], is not accounted for. Moreover, full slip condition with a traction coefficient of 0.4 is assumed for the entire load sequence, resulting in proportional transverse traction and normal contact pressure distributions.

#### 4.1.4. Fatigue crack initiation evaluation

Fatigue crack initiation is assessed using the Dang Van multiaxial fatigue criterion [74], which evaluates the Dang Van fatigue stress based on the interaction between hydrostatic stress and critical plane shear stresses over a loading cycle. This fatigue criterion is often used to evaluate the risk of fatigue crack initiation in loading scenarios with out-of-phase varying stress components [75] and is commonly used in rail-wheel contact evaluation [42,76–78]. The Dang Van stress,  $\sigma_{\rm DV}$ , is computed as:

$$\sigma_{\rm DV}(t) = \tau_{\rm Tr,a}(t) + \langle c_{\rm DV,i} \ \sigma_{\rm h}(t) \rangle > \tau_{\rm e,i} \tag{1}$$

where  $\tau_{e,i}$  is the shear stress fatigue limit for each material phase, with the indexes  $\bullet_i$  denoting each phase accordingly; pearlite:  $\bullet_p$ , martensite:  $\bullet_m$ , bainite:  $\bullet_b$ , tempered martensite or bainite:  $\bullet_t$ . The hydrostatic stress,  $\sigma_h$ , is scaled by the non-dimensional material parameter  $c_{DV,i}$ , with Macaulay brackets  $\langle \bullet \rangle$  omitting non-conservative stress contributions [45]. The Tresca shear stress "amplitude",  $\tau_{Tr,a}$ , is computed from the maximum and minimum principal stresses of the deviatoric stress amplitude tensor  $\underline{\sigma}_{dev,a}$  acting on the critical plane for fatigue crack initiation:

$$\tau_{\text{Tr,a}}(t) = \frac{1}{2} \left( \sigma_{\text{dev,a,I}} - \sigma_{\text{dev,a,III}} \right) \tag{2}$$

For the pearlitic phase, values for  $c_{\text{DV},p}$  and  $\tau_{\text{e,p}}$  are found in the literature [78,79]. For other phases, the fatigue shear stress limits  $\tau_{\text{e},i}$  are estimated by using the pearlite fatigue shear stress limit and the hardness of each phase,  $H_{V,i}$ , measured in repair welding experiments [47], thus partly including ductility effects of the different material phases in possible multi-phase material states:

$$\tau_{\mathrm{e,i}} = \frac{H_{V,i}}{H_{V,p}} \tau_{\mathrm{e,p}} \tag{3}$$

Furthermore,  $c_{DV,i}$  is computed based on fatigue limits on alternating bending and alternating shear using Eq. (1):

$$c_{\mathrm{DV},i} = 3\left(\frac{\tau_{\mathrm{e},i}}{\sigma_{\mathrm{ew},i}} - \frac{1}{2}\right) \tag{4}$$

**Table 2** Fatigue-related material parameters for different phases, assuming a defect size of  $\sqrt{area} = 126 \mu m$  derived from hardness values found in [35–37,47,81] and the R260 fatigue limit found in [79].

	Pearlite	Martensite	Bainite	Tempered
$H_V$ [kgf/mm <sup>2</sup> ]	275	520	420	340
c <sub>DV</sub> [-]	0.33	0.64	0.55	0.44
$\sigma_{\rm ew}$ [MPa]	275	446	376	320
$\tau_{\rm e}$ [MPa]	168	318	257	208

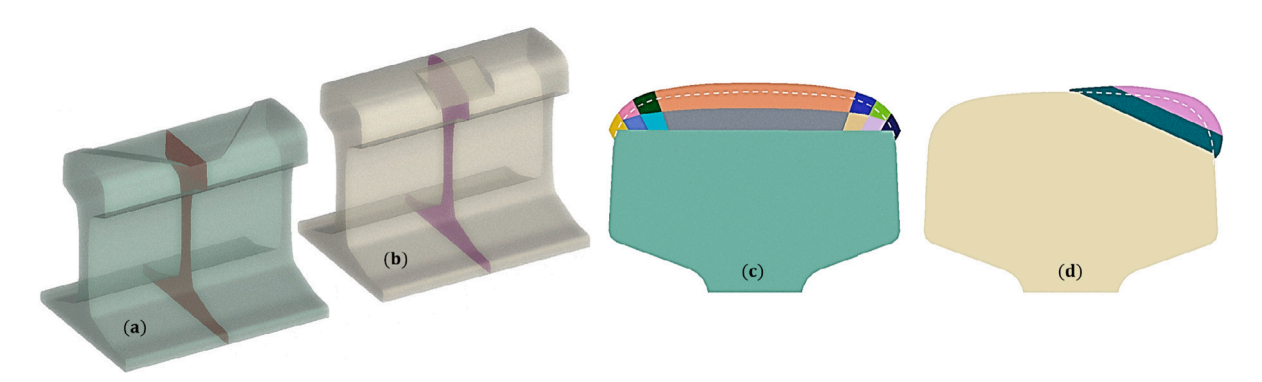


Fig. 4. (a) & (b) 3D FE-models and 2D FE-model cross sections of the regulatory and faulty repair weld procedure, respectively. (c) & (d) Highlight of the 2D railhead FE-models for the regulatory and faulty procedure, respectively, with distinctive colors indicating the different weld passes.

where  $\sigma_{\text{ew},i}$  represents the alternating bending fatigue limit, estimated using Murakami's approach [80] for subsuface cracks:

$$\sigma_{\text{ew},i} = \frac{1.56(H_{V,i} + 120)}{(\sqrt{area})^{1/6}} \tag{5}$$

where the defect parameter  $\sqrt{area}$  represents the size of an inherent subsurface material defect from which the fatigue crack initiates. Based on the fatigue limit in alternating bending for pearlitic R260 rail steel from [79], a defect size of  $\sqrt{area} = 126 \,\mu m$  is obtained, which corresponds well to the size of the defects observed in documented railhead repair welding [36,81]. This defect size is assumed to be representative for the whole welded area, i.e. assumed to be the same for all material phases. Using Eqs. (3)–(5), the material phase specific parameters required in the fatigue stress evaluation are calculated and presented in Table 2. It should be noted that as the hardness values are obtained from rail repair welding, the values are lower than what is typically seen in quenching or thermal flashing studies, see e.g. [82,83]. Furthermore, in line with the multi-phase homogenization-based material modeling, for any multi-phase states obtained in the simulations, fatigue properties used in the Dang Van criterion are computed using a volume-fraction-weighted linear rule of mixtures.

#### 4.2. Simulation setup

#### 4.2.1. FE-model of rail geometries

The finite element (FE) models are based on the European rail profile 60E1 [54]. This subsection describes the mesh characteristics, the differences in cut-out geometries for the faulty and regulatory repairs, and the use of 2D and 3D mechanical and thermal simulations for each repair scenario.

The most obvious distinction between the faulty and regulatory repairs lies in the geometry of the railhead material removal prior to repair welding, as illustrated in Fig. 1. The repairs are performed on the same rail profile, but the cut-out dimensions differ significantly. The faulty repair features a cut-out located only at the gauge corner of the railhead, with dimensions of 50 mm in length, 40 mm in width, and a maximum depth of approximately 10 mm. As discussed in Section 2, this shallow and localized cut-out reflects common deviations observed in field failure reports. In contrast, the regulatory repair follows the specifications outlined in the Swedish railhead stick weld repair regulations, see Section 2. In short, it features a trapezoidal shape, measuring 180 mm at the longer edge, 40 mm at the shorter edge, and a depth of 10 mm.

The 2D cross-sections analyzed in this study correspond to the central-most sections of each repair scenario, as illustrated in Figs. 4a and 4b. These cross-sections are selected to provide a representative view of the residual stress distribution and metallurgical transformations in the repaired railhead. A more detailed visualization of the railhead regions in the 2D models is provided in Figs. 4c and 4d, where the distinct colors illustrate different weld passes. Specifically, for the regulatory repair procedure, as shown in Fig. 4c, the initial longitudinal support weld passes at both edges of the cut-out, followed by zig-zag weld passes in between. And in contrast, the faulty repair procedure, as shown in Fig. 4d, consists solely of slanted zig-zag passes concentrated at the gauge corner.

**Table 3**Double ellipsoid Goldak heat source parameters used for the heat transfer simulations [47].

Heat input	Efficiency Front heat		Rear heat	Rear heat Length parameters				
power $(Q_0)$	$(\eta)$	fraction $(f_f)$	fraction $(f_r)$	a	b	$c_r$	$c_f$	speed
5.25 kW	0.7	0.4	0.6	5.5 mm	4.0 mm	6.0 mm	3.0 mm	3.3 mm/s

The characteristics of the mesh are similar for both faulty and regulatory repair simulations. In the 3D models used for heat transfer analyses, weld layers and heat-affected zone (HAZ) are finely meshed with a characteristic element length of approximately 0.25 mm. In the far-field areas, the mesh is gradually coarsened in both the cross-section and axial directions to optimize computational efficiency. Similarly, the 2D GPS models of the mechanical simulations use the same fine mesh resolution of 0.25 mm in the weld layers and HAZ and a coarser mesh in the rail web and rail foot. This setup ensures mesh convergence such that temperature gradients and residual stress concentrations are adequately resolved in the critical regions. However, for the 3D mechanical simulation of the faulty repair, which is used solely for validation purposes, a characteristic element length of 1 mm is used as a compromise to reduce computational cost.

#### 4.2.2. Welding - Heat transfer simulation

The heat transfer simulations are performed using 3D models, for both the faulty and regulatory repair, to capture the transient temperature fields during the multi-pass repair welding process. The same heat source parameters and boundary conditions are applied for both repair scenarios. Thermal boundary conditions include radiation and convection, which are imposed on all external surfaces of the rail section to ensure realistic heat dissipation during.

To simulate the propane torch preheating before the repair welding process, a surface heat flux of  $60 \text{ kW/m}^2$  is applied to the rail surface for a duration of 500 s. The preheated region extends 100 mm on either side of the cut-out and to the entire rail cross-section. The ambient temperature and initial rail temperature is set to 20 °C, the specified preheating temperature limit is 350 °C and the minimum operational temperature limit is 300 °C.

The heat input from the welding torch is simulated using a moving Goldak heat source model [68], which has been calibrated in previous work [47]. Table 3 summarizes the key parameters of the heat source, including the heat input power, efficiency, front and rear heat fractions, the characteristic dimensions of the heat source ellipsoid, and the traversing speed. The same parameters are used for the faulty and regulatory repairs. However, the initial support ridge weld passes of the regulatory procedure uses about 20% less heat input and about 20% higher traversing speed. Following the welding process, the rail is allowed to cool naturally in ambient conditions, with no forced cooling or post-heat treatment applied.

#### 4.2.3. Welding - mechanical simulation

The temperature field obtained from the heat transfer simulation is mapped onto both the 3D and 2D mechanical models, where it drives phase transformations and thermal expansion in quasi-static simulations. This mapping ensures that the mechanical response, in terms of stress evolution and deformation, reflects the transient thermal response of the welding process. To maintain consistency between the 2D and 3D modeling approaches, the 2D model out-of-plane spring stiffness (see Section 4.1.2) are applied as boundary conditions at each end of the 500 mm rail section analyzed in the 3D model. Additional boundary conditions include fixed constraints applied at the rail foot to prevent rigid body motion.

Following the cooling step, excess weld material at the rail surface (indicated by dotted lines in Figs. 4c and 4d) is removed using the silent element method. This approach deactivates the elements without introducing additional thermal effects from grinding. While this method does not explicitly capture stress changes caused by the surface heating during grinding, it effectively accounts for stress redistribution caused by the geometry change. This simplification is justified, as the heating effects of grinding are confined to very shallow depths at the rail surface, and any associated residual stresses in this region are negligible compared to the subsequent stress redistribution caused by operational over-rolling loads.

#### 4.2.4. Over-rolling simulation

The over-rolling simulations are performed exclusively using the 2D mechanical models to evaluate the mechanical response of the repaired rail under repeated wheel loads, i.e. simulating how the residual stress from welding are redistributed with each over-rolling event using cyclic hardening plasticity material modeling (see Section 4.1.1). Fixed constraints are applied to the rail foot to prevent rigid body motion, while the Hertzian contact pressure distribution and a transverse traction load are applied normal to the rail surface. This setup replicates the rolling motion of a wheel traversing the repaired section by traversing the Hertzian contact patch in the out-of-plane direction. The magnitude of the applied normal load and the corresponding contact position are adjusted for each over-rolling event based on the measured load spectra, as described in Section 4.1.3. The simulated train wheel contact loads are applied to the welded side of the rail for the faulty repair, and to the shorter edge of the trapezoid-shaped weld of the regulatory repair procedure, as illustrated in Fig. 1a.

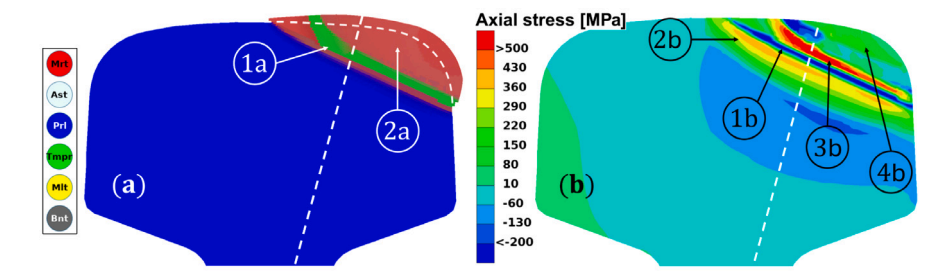


Fig. 5. (a) Illustration of the material phases in the faulty railhead repair. (b) Longitudinal (axial) residual stress distribution obtained from the 2D simulation.

#### 5. Simulation results

This section presents the results of the FE simulations conducted to evaluate the effects of faulty and regulatory railhead repair welding procedures. The evaluation is structured into two primary categories; Firstly, an assessment and comparison of the residual stress fields and material phases of the faulty and regulatory repair welding procedures is presented. Secondly, the mechanical performance of the two procedures is compared and evaluated. Additionally, a validation of the 2D mechanical simulation methodology is presented in Appendix.

#### 5.1. Faulty railhead repair

Fig. 5 presents the predicted residual stress field and resulting material phases for the faulty repair, in the rail cross section highlighted in Figs. 4b and 4d. In Fig. 5a, a rudimentary illustration of the predicted material phases is presented, showing that at the gauge corner, the HAZ experiences rapid cooling, leading to the formation of martensite and some bainite for both the first and second weld layer (illustrated in 4d). Moreover, the figure shows how the heat of the second weld layer tempers some of the martensite formed in the first layer (highlight 1a). The second weld layer primarily consists approximately of 7/10 martensite, 2/10 bainite, and 1/10 retained austenite (highlight 2a), with a lower martensitic fraction than the first layer due to slower cooling. The mixture of brittle and tempered material phases correspond well with observations and measurements obtained from rail welding experiments with similar conditions [47].

The resulting residual stress distribution is illustrated in Fig. 5b (a node value average contour plot). In the first weld layer, the expansion during martensitic transformation induces compressive stresses (highlight 1b), counterbalanced by tensile stresses in the adjacent pearlitic material (highlight 2b). Subsequent tempering of the first-layer martensite leads to shrinkage-induced tensile residual stresses (highlight 3b). In the second weld layer, the accumulated heat results in a higher operating temperature and slower cooling rates, producing a lower martensitic volume fraction and weaker compressive stresses (highlight 4b).

#### 5.2. Regulatory railhead repair

Fig. 6 presents the predicted residual stress field and resulting material phases for the regulatory repair, in the rail cross section highlighted in Figs. 4a and 4c. The simulations clearly show how the high heat input from the powerful zig-zag weld passes produces slower cooling rates, which in turn promotes the formation of a predominantly ferritic-pearlitic microstructure in the weld metal and surrounding HAZ (highlight 1a). Due to the chemical composition of the filler material [56], the exact microstructure constituents differ somewhat from the original pearlitic rail steel [54]. However, for illustrative purposes, the mixed ferritic-pearlitic phase is represented as pearlite in Fig. 6a. Moreover, the figure shows how the non-melted material near the fusion zone of the first zig-zag weld pass forms a crescent-shaped region of approximately 1/12 bainite (highlight 2a).

The residual stress distribution in the regulatory repair, shown in Fig. 6b, exhibits characteristic compressive stresses within the melted and re-solidified weld region (highlight 2b). These compressive stresses result from the thermal contraction of the melted material upon solidification and are counterbalanced by significant tensile stresses beneath the rail surface (highlight 2b). The shape of the residual stress distribution is qualitatively validated through a comparison with other railhead repair welding procedures, both in experimental stress measurements [84,85] and numerical simulations [45,46]. However, it should be noted that the residual stress profile of a repair welded rail differs significantly from that of flash-butt welding, see e.g [86], and thermite welding, see e.g. [43], which typically generates compressive longitudinal stresses at the rail surface.

#### 5.3. Comparing faulty and regulatory repair procedures

#### 5.3.1. Repair welding comparison

As illustrated in Figs. 7a and 7b, a comparative analysis of the simulation outcomes from both the faulty and regulatory repairs reveals a striking contrast in the material state within the weld metal and HAZ. The regulatory repair method yields an almost

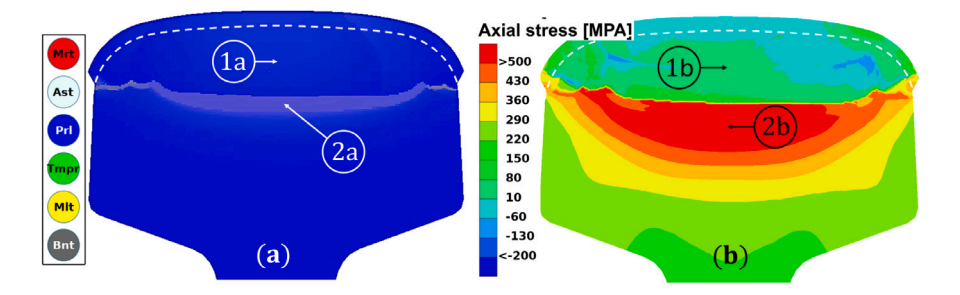


Fig. 6. Repair welded railhead, following the regulatory procedure. Simulation results obtained from 2D simulation: (a) Illustration of the material phases. (b) Longitudinal (axial) residual stress distribution.

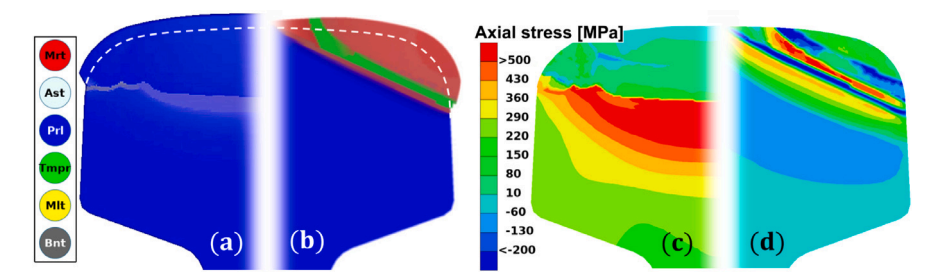


Fig. 7. Repair welded railheads, side-by-side comparison of 2D simulation results: (a) & (b) illustrates the material phases and (c) & (d) presents longitudinal (axial) residual stress fields. (a) & (c) following the regulatory procedure and (b) & (d) following the faulty procedure.

homogeneous ferritic-pearlitic microstructure, attributable to its lower cooling rates that follows the powerful heat input from the zig-zag weld passes. Conversely, the faulty repair produces a mixture of martensite and bainite, resulting from a lower total heat input and faster cooling rates. This difference in phase composition directly impacts mechanical performance, as the material phases of the faulty procedure are significantly more brittle than those of the regulatory procedure. Moreover, it should be noted that in the vicinity of the fusion boundary, partial melting of the base rail material (so-called "mushy zone") may result in compositional gradients of rail and filler material, see Table 1. This dilution is not explicitly modeled in the simulation framework employed, in which compositional gradients are overestimated, resulting in conservative representations of the resulting residual stress states.

A comparison of the residual stress distributions for the regulatory and faulty repairs, as illustrated in Figs. 7c and 7d, reveals fundamental differences in characteristics due to variations in cut-out geometry, weld pass sequence, and heat input. While both procedures generate tensile and compressive residual stress regions, the stress distribution in the regulatory repair is more uniform, with the tensile stress region located deeper below the rail surface, where the microstructure is more homogeneous and less susceptible to fatigue crack imitation. In contrast, the faulty repair demonstrates steeper stress gradients and stronger localized tensile stresses in closer proximity to the surface, increasing its susceptibility to surface-initiated fatigue failures when coinciding with the high-contact stress region during wheel over-rolling.

#### 5.3.2. Operational performance comparison

Fig. 8 presents the residual longitudinal stress field after 2000 over-rollings for three cases: (a) a non-repaired rail used as an illustrative reference, (b) following a regulatory railhead repair, and (c) following a faulty railhead repair. For all three cases, the train wheel flange passes at the right side of the railhead in the figures. As described in Section 2, this is on the shorter edge of the trapezoid-shaped weld of the regulatory repair procedure, as illustrated in Fig. 1a.

Note that the reference case in Fig. 8a is displayed with different color contour limits due to the significantly lower magnitudes of tensile residual stress following over-rollings compared to the residual stress magnitudes induced by the repair welding processes. As shown in the figure, over-rollings induce strong compressive residual stresses at the rail surface, particularly in distinct regions corresponding to the primary contact patch clusters, as identified from field-measured wheel loads [72]. The magnitude and distribution of the over-rolling residual stress field can be qualitatively validated by comparison to experimental measurements in [87] and numerical simulations in [88].

By comparison to the welding residual stresses presented in Figs. 5b and 6b, Figs. 8b and 8c clearly illustrate how the welding-induced residual stresses are redistributed at the rail surface due to high contact pressures from repeated over-rollings (highlights 1b and 1c). However, beneath the rail surface, the residual stress field remains largely unaffected (highlights 2b and 2c), as the material response during over-rollings in these regions remains predominantly elastic. A key observation when comparing the regulatory and faulty repairs is that the localized tensile residual stresses in the faulty repair (highlight 1c) are not redistributed to the same extent as in the regulatory repair (highlight 1b). This outcome can be attributed to the martensitic surface layer (see Fig. 5a), undergoing

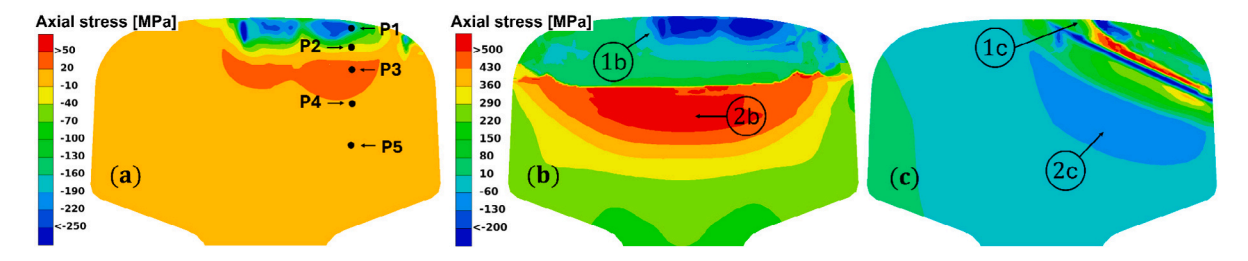


Fig. 8. Residual longitudinal (axial) stress in the railhead after 2000 simulated over-rollings, for three cases: (a) Reference case, non-repaired rail (b) repair welded rail following the regulatory procedure, and (c) following the faulty procedure.

Table 4

Dang Van stress fatigue evaluation of repair welded rail, following the regulatory and faulty welding procedures, under operational over-rolling. Evaluated in the five points highlighted in Fig. 8a.

	Regulatory repair				Faulty repair					
Point	P1	P2	Р3	P4	P5	P1	P2	Р3	P4	P5
H <sub>V</sub> [kgf/mm <sup>2</sup> ]	282	281	279	285	275	494	361	284	275	275
c <sub>DV</sub> [-]	0.34	0.34	0.34	0.35	0.33	0.57	0.47	0.34	0.33	0.33
$\tau_{\rm e}$ [MPa]	172	172	170	174	168	285	220	173	168	168
$\sigma_{\rm DV}$ [MPa]	94	35	73	115	42	167	88	89	86	34
$\eta_{\mathrm{DV}}$ [–]	0.54	0.21	0.43	0.66	0.27	0.59	0.40	0.51	0.51	0.20

less plastic deformation due to its high yield stress. Consequently, the faulty repair retains tensile stresses closer to the rail surface, which, when combined with the presence of brittle material phases, significantly increases the risk of fatigue crack initiation and propagation. An example of this consequence is seen in the rail fracture surface shown in Fig. 3, where the crack appears to have propagated along the tensile stress regions fusion zone.

To further assess the operational mechanical performance of the two repair processes, Table 4 presents the Dang Van fatigue evaluation for the two repair procedures, evaluated at the five points highlighted in Fig. 8a. For both procedures, the material phase volume fractions in each point are used to compute the hardness and the fatigue parameters using a linear rule of mixtures homogenization, indirectly incorporating ductility effects of multi-phase states. The computed hardness values align very well with the measurements presented in [36,47,81].

It is important to note that the Dang Van fatigue criterion is a multiaxial fatigue criterion, and the 2D assumption used in the over-rolling simulations does not fully account for the out-of-plane shear stress components of the stress tensor. Furthermore, the evaluation outcome is governed by the size of the inherent material defect ( $\sqrt{area}$ ) assumed present in all points evaluated and the pearlite fatigue stress limits obtained from [79]. Consequently, the primary focus of the presented Dang Van fatigue stress evaluation is the point-wise comparison of the utilization factor  $\eta_{\rm DV}$  for the regulatory and faulty repair procedure, computed simply as  $\sigma_{\rm DV}/\tau_{\rm e}$ . This qualitative comparison shows how the fatigue performance of the faulty repair is worse or similar in all five points, with the exception of point 4. In this point, the tensile residual stress of the regulatory procedure (highlight 2b in Fig. 6b) causes a significant contribution of hydrostatic stress in the Dang Van stress calculation (Eq. (1)). However, this region is less critical in terms of material defects as it is located some distance from the fusion zone, at the border of the HAZ where the microstructure is homogeneous.

#### 6. Discussion

#### 6.1. Modeling assumptions

The simulation methodology advances the state of the art by integrating a thermo-metallurgical-mechanical welding simulation framework with multi-phase fatigue evaluation. The material model accounts for phase transformation kinetics, cyclic plasticity with isotropic and kinematic hardening, and homogenized multi-phase behavior. Efficiency is achieved through a 2D GPS approach, which reproduces both stress states and phase transformation of 3D simulations at a fraction of the computational cost.

The analysis assumes a stress-free rail prior to repair. In reality, rails contain residual stresses from manufacturing, prior loading, or earlier welds [22]. However, these stresses are largely released during material removal and annealed during repair heating, whereby they are not expected to influence the critical regions identified in this work, namely the added weld material and fusion zone. Similarly, the simplification of neglecting grinding-induced thermal effects is also justified, as they affect only a shallow layer ( $\sim$ 100  $\mu$ m [28,89]) compared to the deeper redistribution caused by repeated wheel–rail loading, as presented in Fig. 8. As both repair scenarios are assessed under the same assumptions, the comparative findings remain valid.

The comparative assessment focused on the center cross-sections of the repair welded rail, which cool more slowly than the edges and therefore provide a conservative basis. Edge sections, particularly in the faulty repair with abrupt weld terminations, cools faster and develops even less favorable microstructures and stresses. The regulatory repair's trapezoidal geometry, by contrast, promotes

gradual heat reduction. Moreover, with the shorter edge facing inwards in track, see Fig. 1, it places critical regions away from direct wheel loading, which is not the case in the faulty procedure. Additional analyses [47] confirm that including edge effects would further increase the discrepancy in performance in favor of the regulatory repair.

Appendix provides a comparison between the 2D GPS model and a 3D mechanical model for the asymmetric geometry of the faulty repair. The general stress trends of the models coincide, as anticipated when driven by the same 3D temperature field. However, transient stress magnitudes differ during high-temperature stages, primarily due to out-of-plane torch (zig-zag) movement and material deposition, as well as temperature-independent 2D stiffness constraints, see Section 4.2.3. Despite under- or overestimated transient fluctuations, it is important to note that the residual stress states converge. For symmetric geometries, as the regulatory repair, the transient correlation is significantly stronger [49]. The 2D model is thus a reliable and efficient computational tool for comparing the two repair procedures.

#### 6.2. Evaluation of fatigue crack initiation risk

The initiation of a fatigue crack is a complex process, often starting from defects in the weld. In this study, initiation is assessed using a multi-phase Dang–Van criterion calibrated to phase hardness and defect sizes observed in service [35,78,81]. To account for realistic defect sizes and microstructural effects, the criterion is linked to the Murakami relation [80]. This framework captures the combined influence of residual stresses, which act as a mean stress, often with a high tensile magnitude, superimposed on cyclic wheel–rail loads, and microstructural properties, which govern local resistance to initiation. Importantly, the scope of this work is focused on evaluating the relative susceptibility to fatigue crack *initiation*, here quantified as when the Dang Van stress amplitude reaches the fatigue stress limit in shear, see Eq. (1). However, for a sufficiently large operational stress range an initiated crack may also *grow*. Residual stresses from the weld will then accelerate the crack growth, as they generally constitute a high tensile mean stress resulting in fully open cracks [90–92]. While this stage lies beyond the scope of the present work, its potentially severe consequences underscore the importance of identifying conditions that promote fatigue crack initiation in repair welds and of implementing effective maintenance strategies.

Based on the above discussion, systematic bias in the fatigue evaluation of the two repair procedures, see Table 4, is unlikely. The main source of uncertainty lies in their respective sensitivity to variations in welding process parameters. Previous work [47] shows that the railhead cut-out geometry has the greatest influence on repair quality, whereas changes in thermal conditions, such as preheating or welding sequence, have comparatively minor effects. Consequently, rerunning the faulty repair with improved thermal conditions, such as adequate preheating or welding sequence, would not significantly change the evaluation outcome. The poor performance of the faulty repair is primarily due to geometric deviations from the regulatory procedure, especially the shallow cut-out depth.

#### 6.3. Rail head repair welding or replacing sections of rails

Placing the present results in the wider context of rail welding practices highlights both opportunities and limitations of insitu railhead repair welding. Compared with more labor-intensive methods of rail repair such as flash-butt welding [39,40,78] and thermite welding [41–43] to replace rail sections, in-situ repair welding offers greater cost-efficiency and reduced operational disruption. However, the localized, heating involved, especially for the faulty procedures, leads to rapid cooling, heterogeneous microstructures, and unfavorable residual stresses. By contrast, flash-butt and thermite welds provide higher and uniform heat input, resulting in slower cooling and more homogeneous microstructures [86], compressive near-surface residual stresses [43,78], and improved fatigue performance, as reflected in lower Dang Van stresses [42]. These differences highlight the inherent trade-off between efficiency and robustness across repair strategies.

#### 7. Conclusion

The present study uses advanced thermo-metallurgical-mechanical finite element simulations to examine the mechanical performance of railhead repair welds under operational loading conditions. A novel modeling framework used to address the critical knowledge gap of how deviations from regulatory repair procedures contribute to the elevated risk of fatigue failure, as observed in field reports. To this end, the regulatory repair welding procedure is compared with a representative faulty procedure in terms of welding residual stresses, stress redistribution during over-rolling and risk of fatigue crack initiation.

This qualitative comparison, based on quantitative data, clearly shows that performing *faulty repairs* substantially *increases* the risk of fatigue crack initiation, as reflected in the following key criteria:

- Microstructure: The regulatory repair produces a predominantly *ferritic–pearlitic microstructure* with sufficient ductility and toughness. In contrast, the faulty repair exhibits *rapid cooling*, resulting in significant formation of *martensite and bainite*, which are more brittle and could be susceptible to crack initiation.
- Residual Stress Field: The regulatory procedure obtains *compressive residual stresses* within the weld region and further down *tensile stresses* in more favorable microstructural zones. The faulty repair, however, develops *strong tensile residual stresses* close to the rail surface, particularly near the gauge corner, which are known from failure reports to be critical for fatigue crack initiation.

- Operational Mechanical Performance: Under simulated over-rolling conditions, the regulatory repair shows *effective stress* redistribution at the rail surface, reducing crack initiation risk. The faulty repair retains surface-near tensile stresses and shows a higher Dang Van fatigue utilization factor ( $\eta_{DV}$ ) across key locations, confirming increased vulnerability to fatigue crack initiation.
- Critical regions: For both procedures, the filler-base material interface are critical regions in terms of are tensile residual stress and material phase gradients. However, for the faulty procedure this region *significantly closer to the rail surface*. Whereas for the regulatory procedure, this region is sub-surface and thereby less affected by operational loading.

These findings are consistent with documented cases of rail fracture and underscore the importance of strict adherence to standard repair welding procedures. Consequently, it is imperative that railway maintenance schedules allocate sufficient time and resources to avoid incentivizing the use of faster, but detrimental faulty repair welding techniques.

#### **CRediT** authorship contribution statement

**Björn Andersson:** Writing – original draft, Visualization, Validation, Project administration, Methodology, Investigation, Formal analysis, Data curation, Conceptualization. **B. Lennart Josefson:** Writing – review & editing, Supervision, Funding acquisition, Conceptualization.

#### Declaration of Generative AI and AI-assisted technologies in the writing process

The authors employed the Deepl writing assistance tool during the preparation of the present work in order to enhance the language and readability. Following the utilization of this tool, the authors conducted a review and edit of the content, taking full responsibility for the publication's content.

#### Declaration of competing interest

The authors declare that they have no known competing financial interests or personal relationships that could have appeared to influence the work reported in this paper.

#### Acknowledgments and funding

The authors kindly express their gratitude to Professor Anders Ekberg of Chalmers University of Technology for his valuable discussions regarding the multi-axial fatigue crack initiation evaluation. Additionally, the authors would like to express their sincere appreciation to Mr. Stefan Kallander of the Swedish Traffic Administration for generously sharing his expertise on in-field rail repair welding procedures.

The current study is part of the ongoing activities in CHARMEC – Chalmers Railway Mechanics (www.chalmers.se/charmec). Through CHARMEC, the study have been funded from the Horizon Europe research and innovation programme IAM4RAIL - FP3 under grant agreement number 101101966. Moreover, the numerical simulations were performed on resources provided by Chalmers e-Commons (C3SE).

#### Appendix. Validation of 2D simulation methodology using 3D model

#### A.1. Residual stress field comparison

For symmetric repair welding geometries, the simulation methodology emplyed is validated in [49]. To validate the accuracy of the 2D simulation methodology also for the asymmetric faulty repair procedure, 2D mechanical simulation results are compared with those obtained from a 3D mechanical simulation. As the 2D model represents the central cross-section of the repaired rail (see Fig. 4b), only results from the corresponding cross-section in the 3D model are considered. Figs. 5b and A.9c presents the longitudinal residual stress field in the railhead predicted by the 2D and 3D mechanical simulations. Comparing the results demonstrates that the 2D simulation effectively reproduces the overall stress trends observed in the 3D simulation, capturing the stress distribution gradients and key mechanical responses of the HAZ. However, due to the finer FE mesh resolution in the 2D model, higher peak stress magnitudes are observed in both compressive and tensile stress regions when compared to the 3D results. The immense computational cost of the 3D mechanical simulation prevents the use of finer mesh, and thus the same level of mesh convergence as for the 2D mechanical simulation, in terms of the residual stresses, is not obtainable.

Furthermore, a quantitative comparison of the major principal stress distribution is provided by the graph presented in Fig. A.9a. The graph plots the principal stresses (nodal value average) along the diagonal white dashed lines indicated in Figs. 5 and A.9c. These stress paths extend to the center of the rail foot and the rail cross-section illustrated in light gray. As the longitudinal stress component is the dominant stress component, the magnitude and overall trend of the major principal stress are very similar, as can be seen by comparing the graph and the stress field (Figs. A.9a and 5b). Moreover, the graph confirms that the 2D model accurately captures the general stress trends predicted by the 3D simulation in the HAZ. However, as observed in the stress field comparison, higher peak values are present in the 2D model.

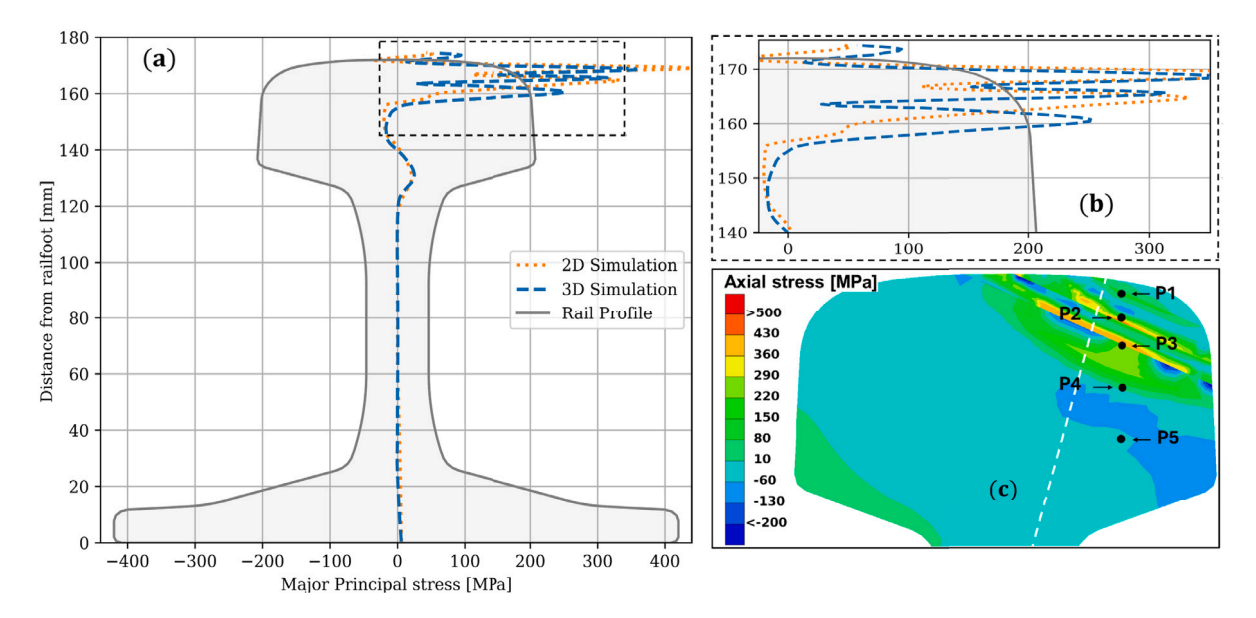


Fig. A.9. (a) & (b) Comparison of major principal stress variations along the reference path highlighted in Fig. 5. (c) 3D simulation results, axial stress (longitudinal (axial) stress component).

In summary, while discrepancies in peak stress magnitudes are observed due to mesh refinement differences, the findings indicate a satisfactory correlation between the 2D and 3D simulations for the critical parameters governing repair quality, specifically the intensity and distribution of the longitudinal residual stress field. The 2D model successfully replicates the residual stress field observed in the 3D simulation, thereby confirming its suitability as a computationally efficient, valid, and practical alternative for analyzing repair welding procedures.

#### A.2. Transient time-stress history comparison

To further evaluate the consistency between the 2D and 3D simulation models, the transient evolution of the longitudinal stress component is analyzed. Fig. A.10 presents the stress-time history at five locations (P1 to P5) in the railhead, as indicated in Fig. 8c. Four key time instances of the repair welding process are highlighted in the figure; (a) deposition of the first weld layer, (b) repositioning of the welding torch, (c) deposition of the second weld layer, and (d) final cooling to ambient temperature.

As illustrated by the graphs, the impact of temperature-induced phase transformations on the stress history is evident. Under relatively monotonic heating conditions (instances a and c), sequential transformations induce cyclic strain, as detailed in e.g. [93]. Additionally, the stress-time history demonstrates the significance of virgin material state recovery, as indicated by the similarity in stress response between post-solidification stages (instances a and c for Point 1). Furthermore, for the weld filler material (Points 1), the longitudinal residual stress approaches the material's yield strength, which aligns with established welding mechanics literature, see e.g. [94]. However, due to the presence of a heterogeneous phase mixture, a direct comparison is complex.

The comparison reveals that the general stress evolution trends in the 2D and 3D mechanical models are similar, which is expected since both models driven by the same transient thermal field. However, the magnitude of the transient stresses varies significantly during some high temperature stages of the simulations. In particular, during weld deposition (instances a and c), the 3D model exhibits larger stress fluctuations, which most can be attributed to zig-zag movement of the weld torch occurring outside of the 2D cross-section considered. The overall dependency is likely due to the GPS assumptions of the 2D model in combination with the temperature-independent out-of-plane stiffness constraints, as described in Section 4.1.2. Furthermore, the in-plane asymmetry of the faulty repair geometry is an additional contributor to this discrepancy, explaining the discrepancies in points 4 and 5 that start during the first heating cycle. These inherent 2D simplifications may limit the model's ability to fully capture the dynamic redistribution of stresses. The limitations associated with the asymmetric geometry of the faulty repair become particularly evident when considering the 2D model validation of the symmetric rail repair weld geometry presented in [49], where the transient 3D correlation is significantly stronger.

Despite these differences in transient stress responses, a key observation is that as cooling progresses (instance d), the residual stress predictions of the 2D model gradually converge towards those of the 3D model. This suggests that while the 2D model may overestimate or underestimate stress variations during intermediate stages, it still adequately captures the residual stress state.

#### Data availability

Data will be made available on request.

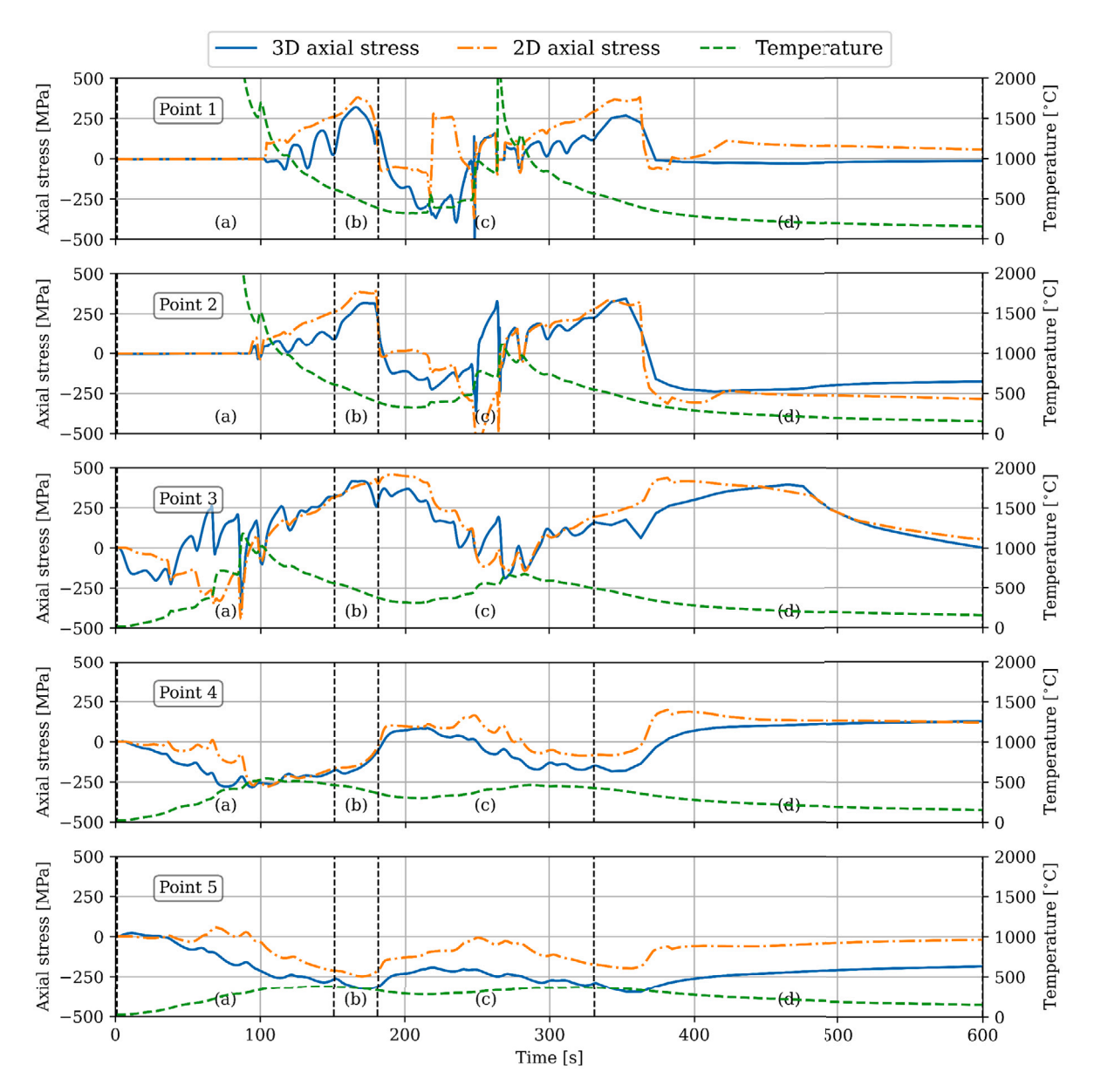


**Fig. A.10.** Comparison the time history of longitudinal (axial) stress component of 2D and 3D repair welding simulations for the faulty procedure. Measured at locations P1 to P5 highlighted in Fig. A.9. Four time instances are highlighted in each graph: (a) deposition of the first weld layer, (b) repositioning of the welding torch, (c) deposition of the second weld layer, and (d) final cooling to ambient temperature.

#### References

- [1] C. Doll, C. Brauer, J. Köhler, P. Scholten, Methodology for GHG Efficiency of Transport Modes, Tech. Rep., Fraunhofer-Institute for Systems and Innovation Research ISI, Karlsruhe, Germany, 2020.
- [2] White Paper: Roadmap to a Single European Transport Area Towards a Competitive and Resource Efficient Transport System, Tech. Rep., European Commission (EC), Brussels, 2011.
- [3] United Nations General Assembly, The sustainable development goals report 2023: Special edition, 2023.
- [4] A. Ekberg, Fatigue of railway wheels, in: R. Lewis, U. Olofsson (Eds.), Wheel-Rail Interface Handbook, Woodhead Publishing, 2009, pp. 211–244, http://dx.doi.org/10.1533/9781845696788.1.211.
- [5] S.M. Famurewa, A. Nissen, U. Kumar, Scheduling of railway infrastructure maintenance tasks using train free windows, in: Current Trends in Reliability, Availability, Maintainability and Safety, Springer International Publishing, Cham, 2016, pp. 425–436, http://dx.doi.org/10.1007/978-3-319-23597-4\_30.
- [6] L. Ferreira, M.H. Murray, Modelling rail track deterioration and maintenance: current practices and future needs, Transp. Rev. 17 (3) (1997) 207–221, http://dx.doi.org/10.1080/01441649708716982.

- [7] P. Larsson-Kråik, Managing the wheel-rail interface: Railway infrastructure maintenance in a severe environment: The Swedish experience, in: R. Lewis, U. Olofsson (Eds.), Whee-Rail Interface Handbook, Woodhead Publishing, 2009, pp. 633–652, http://dx.doi.org/10.1533/9781845696788.2.634.
- [8] T. Zhou, Development of in-suit welding technique to repair rail welded joint with defect, J. Mech. Civ. Eng. (IOSR-JMCE) 17 (3) (2020) 44–51, http://dx.doi.org/10.9790/1684-1703024451.
- [9] B. Dahl, B. Mogard, B. Gretoft, B. Ulander, Repair of rails on-site by welding, Svetsaren 50 (1995) 10-14.
- [10] Banöverbyggnad Svetsning, bearbetning och smörjning, Tech. Rep. TRVINFRA-00016, Trafikverkets infrastrukturregelverk, Borlänge, Sweden, 2022.
- [11] Railway Applications Track Restoration of Rails by Electric Arc Welding. EN 15594:2009(E), European Committee for Standardization (CEN), Brussels, 2009.
- [12] D.F. Cannon, K.-O. Edel, S.L. Grassie, K. Sawley, Rail defects: an overview, Fatigue Fract. Eng. Mater. Struct. 26 (10) (2003) 865–886, http://dx.doi.org/10.1046/i.1460-2695.2003.00693.x.
- [13] E. Kabir, I. Bopda, Rälfel och rälsbrott 2022 Årlig uppföljningsrapport, Tech. Rep., Swedish Traffick Administration, Stockholm, Sweden, 2022.
- [14] M.A. Arslan, O. Kayabaşı, 3-D rail-wheel contact analysis using FEA, Adv. Eng. Softw. 45 (1) (2012) 325-331, http://dx.doi.org/10.1016/j.advengsoft.
- [15] A. Kapoor, F. Franklin, S. Wong, M. Ishida, Surface roughness and plastic flow in rail wheel contact, Wear 253 (1) (2002) 257–264, http://dx.doi.org/10. 1016/S0043-1648(02)00111-4. CM2000 S.L.
- [16] H. Brunskill, A. Hunter, L. Zhou, R.D. Joyce, R. Lewis, An evaluation of ultrasonic arrays for the static and dynamic measurement of wheel-rail contact pressure and area. Proc. Inst. Mech. Eng. Part J: J. Eng. Tribol. 234 (10) (2020) 1580–1593. http://dx.doi.org/10.1177/1350650120919889.
- [17] M.N. Tawfik, M.M. Padzi, S. Abdullah, D. Harmanto, M. Firdaws, H. Hapaz, A review of the rolling contact fatigue of rail wheels under various stresses, J. Fail. Anal. Prev. 23 (1) (2023) 16–29, http://dx.doi.org/10.1007/s11668-022-01568-6.
- [18] S. Jiménez, L. Barbu, S. Oller, A. Cornejo, On the numerical study of fatigue process in rail heads by means of an isotropic damage based high-cycle fatigue constitutive law, Eng. Fail. Anal. 131 (2022) 105915, http://dx.doi.org/10.1016/j.engfailanal.2021.105915.
- [19] J. Zhang, C. Cai, S. Zhu, M. Wang, Q. He, S. Yang, W. Zhai, Experimental investigation on dynamic performance evolution of double-block ballastless track under high-cycle train loads, Eng. Struct. 254 (2022) 113872, http://dx.doi.org/10.1016/j.engstruct.2022.113872.
- [20] M. Loidolt, S. Marschnig, Weld battering of thermite welds and flash butt welds based on statistical evaluations, Eng. Fail. Anal. (2025) 109457, http://dx.doi.org/10.1016/j.engfailanal.2025.109457.
- [21] W. Li, G. Xiao, Z. Wen, X. Xiao, X. Jin, Plastic deformation of curved rail at rail weld caused by train-track dynamic interaction, Wear 271 (1) (2011) 311–318, http://dx.doi.org/10.1016/j.wear.2010.10.002.
- [22] B.L. Josefson, Welding of rails and effects on crack initiation and propagation, in: Encyclopedia of Thermal Stresses, Springer Netherlands, Dordrecht, 2014, pp. 6589–6594, http://dx.doi.org/10.1007/978-94-007-2739-7\_957.
- [23] U. Zerbst, Application of fracture mechanics to welds with crack origin at the weld toe: A review part 1: Consequences of inhomogeneous microstructure for materials testing and failure assessment, Weld. World 63 (6) (2019) 1715–1732, http://dx.doi.org/10.1007/s40194-019-00801-5.
- [24] G. Budai, D. Huisman, R. Dekker, Scheduling preventive railway maintenance activities, J. Oper. Res. Soc. 57 (9) (2006) 1035–1044, http://dx.doi.org/10.1057/palgrave.jors.2602085.
- [25] A. Ekberg, P. Edlund, Concluding Technical Report, In2Track3, Cost-Efficient and Reliablehigh-Capacity Infrastructure, Chalmers University of Technology & Trafikverket, Göteborg, 2024.
- [26] E. Mortazavian, Z. Wang, H. Teng, Finite element investigation of thermal-kinetic-mechanical evolutions during laser powder deposition as an innovative technique for rail repair, Int. J. Adv. Manuf. Technol. 118 (1) (2022) 319–342, http://dx.doi.org/10.1007/s00170-021-07873-y.
- [27] E. Mortazavian, Z. Wang, H. Teng, Finite element investigation of residual stresses during laser powder deposition process as an innovative technique to repair worn rails, Proc. Inst. Mech. Eng. Part F: J. Rail Rapid Transit 237 (1) (2023) 21–32, http://dx.doi.org/10.1177/09544097221089410.
- [28] M. Mesaritis, P. Cuervo, J. Santa, A. Toro, R. Lewis, Assessment of rail grinding maintenance surface quality and damage propagation in subsequent loading cycles for premium rail grades, Wear 530–531 (2023) 205051, http://dx.doi.org/10.1016/j.wear.2023.205051.
- [29] W. Kubin, W. Daves, R. Stock, Analysis of rail milling as a rail maintenance process: Simulations and experiments, Wear 438–439 (2019) 203029, http://dx.doi.org/10.1016/j.wear.2019.203029.
- [30] R.R. Porcaro, G.L. Faria, L.B. Godefroid, G.R. Apolonio, L.C. Cândido, E.S. Pinto, Microstructure and mechanical properties of a flash butt welded pearlitic rail. J. Mater. Process. Technol. 270 (2019) 20–27. http://dx.doi.org/10.1016/j.imatprotec.2019.02.013.
- [31] S. Fischer, D. Harangozó, D. Németh, B. Kocsis, M. Sysyn, D. Kurhan, A. Brautigam, Investigation of heat-affected zones of thermite rail weldings, Facta Univ. Ser.: Mech. Eng. (2024) 689–710.
- [32] S.-H. Lee, S.H. Kim, Y.-S. Chang, H.K. Jun, Fatigue life assessment of railway rail subjected to welding residual and contact stresses, J. Mech. Sci. Technol. 28 (11) (2014) 4483–4491, http://dx.doi.org/10.1007/s12206-014-1016-3.
- [33] A. Allie, H. Aglan, M. Fateh, Microstructure-fracture behavior relationships of slot-welded rail steels, Met. Mater. Trans. A 42 (9) (2011) 2706–2715, http://dx.doi.org/10.1007/s11661-011-0665-4.
- [34] C. Feddersen, R. Buchheit, D. Broek, et al., Fatigue Crack Propagation in Rail Steels, Tech. Rep., United States. Federal Railroad Administration, 1977.
- [35] J. Forsberg, M. Hellsing, Undersö"kning av rälspricka, Odenplan spårväxel 441, Tech. Rep. m2312-5349, Materiex, Borlänge, Sweden, 2024.
- [36] J. Forsberg, T. Widelund, Undersökning av rälsbrott, Rotebro växel 101, Tech. Rep. m2109-4807, Materiex, Borlänge, Sweden, 2021.
- [37] J. Forsberg, M. Hellsing, Undersökning av rälspricka, Bandel 434 Ofelia, Tech. Rep. m2412-5533, Materiex, Borlänge, Sweden, 2025.
- [38] A. Skyttebol, B.L. Josefson, Numerical simulation of flash-butt-welding of railway rail, in: Mathematical Modelling of Weld Phenomena, vol. 7, TU Graz Publication, Graz, Austria, 2004, p. 21.
- [39] L. Godefroid, G. Faria, L. Cândido, T. Viana, Failure analysis of recurrent cases of fatigue fracture in flash butt welded rails, Eng. Fail. Anal. 58 (2015) 407–416, http://dx.doi.org/10.1016/j.engfailanal.2015.05.022, Recent case studies in Engineering Failure Analysis.
- [40] H. Su, C.L. Pun, P. Mutton, Q. Kan, G. Kang, W. Yan, Numerical study on the ratcheting performance of rail flash butt welds in heavy haul operations, Int. J. Mech. Sci. 199 (2021) 106434, http://dx.doi.org/10.1016/j.ijmecsci.2021.106434.
- [41] X. Shi, Y. Liu, Z. Liu, H.J. Hoh, K.S. Tsang, J.H.L. Pang, An integrated fatigue assessment approach of rail welds using dynamic 3D FE simulation and strain monitoring technique, Eng. Fail. Anal. 120 (2021) 105080, http://dx.doi.org/10.1016/j.engfailanal.2020.105080.
- [42] Z. Liu, X. Shi, K. Tsang, H. Hoh, J. Pang, Dynamic finite element modeling and fatigue damage analysis of thermite welds, Fatigue Fract. Eng. Mater. Struct. 43 (1) (2020) 119–136, http://dx.doi.org/10.1111/ffe.13091.
- [43] B.L. Josefson, R. Bisschop, M. Messaadi, J. Hantusch, Residual stresses in thermite welded rails: significance of additional forging, Weld. World 64 (7) (2020) 1195–1212, http://dx.doi.org/10.1007/s40194-020-00912-4.
- [44] J. Jaiswal, S.F. Smith, R. Cox, E. Kabo, Repair of discrete rail head defects a novel technology, in: Collection of Open Conferences in Research Transport, Zenodo, 2018, pp. 1–10, http://dx.doi.org/10.5281/zenodo.1473576.
- [45] E. Kabo, A. Ekberg, M. Maglio, Rolling contact fatigue assessment of repair rail welds, Wear 436–437 (2019) 203030, http://dx.doi.org/10.1016/j.wear. 2019.203030.
- [46] H.K. Jun, D.W. Kim, I.S. Jeon, S.H. Lee, Y.S. Chang, Investigation of residual stresses in a repair-welded rail head considering solid-state phase transformation, Fatigue Fract. Eng. Mater. Struct. 40 (7) (2017) 1059–1071, http://dx.doi.org/10.1111/ffe.12564.
- [47] B. Andersson, E. Steyn, M. Ekh, B.L. Josefson, Simulation-based assessment of railhead repair welding process parameters, Weld. World 69 (2025) 177–197, http://dx.doi.org/10.1007/s40194-024-01837-y.

- [48] B. Andersson, J. Ahlström, M. Ekh, B.L. Josefson, Homogenization based macroscopic model of phase transformations and cyclic plasticity in pearlitic steel, J. Therm. Stresses 45 (6) (2022) 470–492, http://dx.doi.org/10.1080/01495739.2022.2056557.
- [49] B. Andersson, M. Ekh, B.L. Josefson, Computationally efficient simulation methodology for railway repair welding: Cyclic plasticity, phase transformations and multi-phase homogenization, J. Therm. Stresses 47 (2) (2024) 164–188, http://dx.doi.org/10.1080/01495739.2023.2283309.
- [50] A. Esmaeili, J. Ahlström, B. Andersson, M. Ekh, Modelling of cyclic plasticity and phase transformations during repeated local heating events in rail and wheel steels, Int. J. Fatigue 151 (2021) 106361, http://dx.doi.org/10.1016/j.ijfatigue.2021.106361.
- [51] B. Andersson, E. Steyn, J. Ahlström, Thermal pulses on pearlitic steels: Influence of laser heat scanning parameters on surface layers transforming to martensite, Mater. Des. 256 (2025) 114199, http://dx.doi.org/10.1016/j.matdes.2025.114199.
- [52] Svetsning av räler och rälskomponenter. Svetsarprövning, Tech. Rep. TDOK 2014:0587, Trafikverkets infrastrukturregelverk, Borlänge, Sweden, 2018.
- [53] Svetsning av r\u00e4ler och r\u00e4lskomponenter. Godk\u00e4nnande av svetsprocedurer, Tech. Rep. TDOK 2014:0586, Trafikverkets infrastrukturregelverk, Borl\u00e4nge, Sweden, 2018.
- [54] Railway Applications. Track. Rail. Vignole Railway Rails 46 Kg/m and above, BS EN 13674-1:2011+A1:2017, European Committee for Standardization (CEN), Brussels, 2011.
- [55] Banöverbyggnad Oförstörande provning, Tech. Rep. TRVINFRA-00015, Trafikverkets infrastrukturregelverk, Borlänge, Sweden, 2020.
- [56] ESAB, OK weartrode 30, 2023, esab.com/no/eur sv/products-solutions/product/filler-metals/hardfacing/stick-electrodes-smaw/ok-weartrode-30,
- [57] Welding Consumables. Welding consumables for Hard-Facing. BS EN 14700:2022, European Committee for Standardization (CEN), Brussels, 2022.
- [58] R.A. Lebensohn, P.A. Turner, J.W. Signorelli, G.R. Canova, Calculation of intergranular stresses based on a large-strain viscoplastic self-consistent polycrystal model, Modelling Simul. Mater. Sci. Eng. 6 (April 1998) (1998) 447–465, http://dx.doi.org/10.1088/0965-0393/6/4/011.
- [59] R.A. Lebensohn, C.N. Tomé, P.P. Castañeda, Self-consistent modelling of the mechanical behaviour of viscoplastic polycrystals incorporating intragranular field fluctuations, Phil. Mag. 87 (28) (2007) 4287–4322, http://dx.doi.org/10.1080/14786430701432619.
- [60] R. Mahnken, A. Schneidt, T. Antretter, Macro modelling and homogenization for transformation induced plasticity of a low-alloy steel, Int. J. Plast. 25 (2) (2009) 183–204, http://dx.doi.org/10.1016/j.ijplas.2008.03.005.
- [61] J. Chaboche, Constitutive equations for cyclic plasticity and cyclic viscoplasticity, Int. J. Plast. 5 (3) (1989) 247–302, http://dx.doi.org/10.1016/0749-6419(89)90015-6.
- [62] C.O. Frederick, P.J. Armstrong, A mathematical representation of the multiaxial bauschinger effect, Mater. High Temp. 21 (1) (2014) 1–26, http://dx.doi.org/10.1179/096034007X207589.
- [63] J. Leblond, G. Mottet, J. Devaux, A theoretical and numerical approach to the plastic behaviour of steels during phase transformations—II. Study of classical plasticity for ideal-plastic phases, J. Mech. Phys. Solids 34 (4) (1986) 411–432, http://dx.doi.org/10.1016/0022-5096(86)90010-4.
- [64] F. Fischer, G. Reisner, E. Werner, K. Tanaka, G. Cailletaud, T. Antretter, A new view on transformation induced plasticity (TRIP), Int. J. Plast. 16 (7) (2000) 723–748, http://dx.doi.org/10.1016/S0749-6419(99)00078-9.
- [65] M. Chiumenti, M. Cervera, A. Salmi, C. Agelet de Saracibar, N. Dialami, K. Matsui, Finite element modeling of multi-pass welding and shaped metal deposition processes, Comput. Methods Appl. Mech. Engrg. 199 (37) (2010) 2343–2359, http://dx.doi.org/10.1016/j.cma.2010.02.018.
- [66] P. Dong, On repair weld residual stresses and significance to structural integrity, Weld. World 62 (2) (2018) 351–362, http://dx.doi.org/10.1007/s40194-018-0554-1
- [67] Abaqus Analysis User's Manual, two thousand and eighteen ed., Dassault Systèmes Simulia Corp, Providence, Rhode Island USA, 2018.
- [68] J. Goldak, A. Chakravarti, M. Bibby, A new finite element model for welding heat sources, Met. Trans. B 15 (June) (1984) 299–305, http://dx.doi.org/ 10.1007/BF02667333.
- [69] L.-E. Lindgren, Finite element modeling and simulation of welding part 1: Increased complexity, J. Therm. Stresses 24 (2) (2001) 141–192, http://dx.doi.org/10.1080/01495730150500442.
- [70] N. Talebi, B. Andersson, M. Ekh, K.A. Meyer, Influence of a highly deformed surface layer on RCF predictions for rails in service, Wear 578–579 (2025) 206173, http://dx.doi.org/10.1016/j.wear.2025.206173.
- [71] R. Skrypnyk, M. Ekh, J. Nielsen, B. Pålsson, Prediction of plastic deformation and wear in railway crossings comparing the performance of two rail steel grades, Wear 428–429 (2019) http://dx.doi.org/10.1016/j.wear.2019.03.019.
- [72] C. Ansin, B. Pålsson, M. Ekh, F. Larsson, R. Larsson, Simulation and field measurements of the long-term rail surface damage due to plasticity, wear and surface rolling contact fatigue cracks in a curve, in: Proceedings of the 12th International Conference on Contact Mechanics and Wear of Rail/Wheel Systems, 2022, pp. 591–601.
- [73] X. Liu, C. Liu, W. Wu, J. Liu, S. Sun, Y. Wei, Transient dynamics of a full wheel rail set passing a weld irregularity at high speed, Eng. Fail. Anal. 148 (2023) 107203, http://dx.doi.org/10.1016/j.engfailanal.2023.107203.
- [74] K. Dang Van, G. Cailletaud, J. Flavenot, A. Le Douaron, H. Lieurade, Criterion for high cycle fatigue failure under multiaxial loading, in: International Conference on Biaxial/Multiaxial Fatigue, Mechanical Engineering Publications, University of Sheffield, 1985, pp. 479–496.
- [75] K. Dang-Van, Macro-micro approach in high-cycle multiaxial fatigue, in: Advances in Multiaxial Fatigue, ASTM International, 1993, pp. 120–130, http://dx.doi.org/10.1520/STP24799S.
- [76] A. Ekberg, E. Kabo, H. Andersson, An engineering model for prediction of rolling contact fatigue of railway wheels, Fatigue Fract. Eng. Mater. Struct. 25 (10) (2002) 899–909, http://dx.doi.org/10.1046/j.1460-2695.2002.00535.x.
- [77] M. Ciavarella, F. Monno, G. Demelio, On the dang van fatigue limit in rolling contact fatigue, Int. J. Fatigue 28 (8) (2006) 852–863, http://dx.doi.org/10.1016/j.ijfatigue.2005.11.002.
- [78] B.L. Josefson, J.W. Ringsberg, Assessment of uncertainties in life prediction of fatigue crack initiation and propagation in welded rails, Int. J. Fatigue 31 (8) (2009) 1413–1421, http://dx.doi.org/10.1016/j.ijfatigue.2009.03.024.
- [79] B.L. Josefson, J.W. Ringsberg, Assessment of uncertainties in life prediction of fatigue crack initiation in rails-influence of residual stresses from manufacturing, in: Proceedings of the Eighth International Conference on Multiaxial Fatigue & Fracture (8th ICMF&F) in Sheffield, UK, June 10-14, 2007, 2007, pp. 1–8.
- [80] Y. Murakami, M. Endo, Effects of defects, inclusions and inhomogeneities on fatigue strength, Int. J. Fatigue 16 (3) (1994) 163–182, http://dx.doi.org/10.1016/0142-1123(94)90001-9.
- [81] D. Franklin, A. Lundstjälk, LIVAR Livslängsoptimering av räler, Tech. Rep., Swerim, Stockholm, Sweden, 2021.
- [82] V. Mattos Ferreira, M. Mecozzi, R. Petrov, J. Sietsma, Microstructure development of pearlitic railway steels subjected to fast heating, Mater. Des. 221 (2022) 110989, http://dx.doi.org/10.1016/j.matdes.2022.110989.
- [83] M. Freisinger, H. Rojacz, K. Pichelbauer, A. Trausmuth, G. Trummer, K. Six, P. Mayrhofer, Comparative study on the influence of initial deformation and temperature of thermally induced white etching layers on rail wheels, Tribol. Int. 177 (2023) 107990, http://dx.doi.org/10.1016/j.triboint.2022.107990.
- [84] H.-K. Jun, J.-W. Seo, I.-S. Jeon, S.-H. Lee, Y.-S. Chang, Fracture and fatigue crack growth analyses on a weld-repaired railway rail, Eng. Fail. Anal. 59 (2016) 478–492. http://dx.doi.org/10.1016/j.engfailanal.2015.11.014.
- [85] Y. Sun, G. Obasi, C. Hamelin, A. Vasileiou, T. Flint, J. Francis, M. Smith, Characterisation and modelling of tempering during multi-pass welding, J. Mater. Process. Technol. 270 (2019) 118–131, http://dx.doi.org/10.1016/j.jmatprotec.2019.02.015.
- [86] Y. Pang, N. Grilli, H. Su, W. Liu, J. Ma, S.F. Yu, Experimental investigation on microstructures and mechanical properties of PG4 flash-butt rail welds, Eng. Fail. Anal. 141 (2022) 106650, http://dx.doi.org/10.1016/j.engfailanal.2022.106650.

- [87] P. Webster, X. Wang, G. Mills, G. Webster, Residual stress changes in railway rails, Phys. B 180–181 (1992) 1029–1031, http://dx.doi.org/10.1016/0921-4526(92)90541-Y
- [88] J.W. Ringsberg, T. Lindbäck, Rolling contact fatigue analysis of rails inculding numerical simulations of the rail manufacturing process and repeated wheel-rail contact loads, Int. J. Fatigue 25 (6) (2003) 547–558, http://dx.doi.org/10.1016/S0142-1123(02)00147-0.
- [89] C. Zhao, J. Li, W. Fan, Y. Liu, W. Wang, Experimental and simulation research on residual stress for abrasive belt rail grinding, Int. J. Adv. Manuf. Technol. 109 (2020) 129–142, http://dx.doi.org/10.1007/s00170-020-05664-5.
- [90] N.E. Dowling, S.L. Kampe, M.V. Kral, Mechanical Behavior of Materials: Engineering Methods for Deformation, Fracture, and Fatigue, fifth ed., Pearson Education, United Kingdom, 2020.
- [91] Y. Li, P. Mutton, C. Qiu, Q. Kan, W. Yan, Residual stress and its effect on ratcheting of heavy-haul rails, Eng. Fail. Anal. 170 (2025) 109254, http://dx.doi.org/10.1016/j.engfailanal.2024.109254.
- [92] A. Skyttebol, B. Josefson, J. Ringsberg, Fatigue crack growth in a welded rail under the influence of residual stresses, Eng. Fract. Mech. 72 (2) (2005) 271–285, http://dx.doi.org/10.1016/j.engfracmech.2004.04.009, Fracture Mechanics in Railway Applications.
- [93] C. Şimşir, C.H. Gür, A simulation of the quenching process for predicting temperature, microstructure and residual stresses, Stroj. Vestn. / J. Mech. Eng. 56 (2) (2010) 93–103.
- [94] K. Masubuchi, Analysis of Welded Structures: Residual Stresses, Distortion, and Their Consequences, first ed., Pergamon Press Inc., Elmsford (New York), 1980, http://dx.doi.org/10.1016/C2013-0-05818-5.